

Machine learning-based identification of *Gaia* astrometric exoplanet orbits

Johannes Sahlmann^{1*} and Pablo Gómez^{2†}

¹*RHEA Group for the European Space Agency (ESA), European Space Astronomy Centre (ESAC), Camino Bajo del Castillo s/n, 28692 Villanueva de la Cañada, Madrid, Spain*

²*European Space Agency (ESA), European Space Astronomy Centre (ESAC), Camino Bajo del Castillo s/n, 28692 Villanueva de la Cañada, Madrid, Spain*

Accepted XXX. Received YYY; in original form ZZZ

ABSTRACT

The third *Gaia* data release (DR3) contains ~170 000 astrometric orbit solutions of two-body systems located within ~500 pc of the Sun. Determining component masses in these systems, in particular of stars hosting exoplanets, usually hinges on incorporating complementary observations in addition to the astrometry, e.g. spectroscopy and radial velocities. Several DR3 two-body systems with exoplanet, brown-dwarf, stellar, and black-hole components have been confirmed in this way. We developed an alternative machine learning approach that uses only the DR3 orbital solutions with the aim of identifying the best candidates for exoplanets and brown-dwarf companions. Based on confirmed substellar companions in the literature, we use semi-supervised anomaly detection methods in combination with extreme gradient boosting and random forest classifiers to determine likely low-mass outliers in the population of non-single sources. We employ and study feature importance to investigate the method’s plausibility and produced a list of 22 best candidates of which four are exoplanet candidates and another five are either very-massive brown dwarfs or very-low mass stars. Three candidates, including one initial exoplanet candidate, correspond to false-positive solutions where longer-period binary star motion was fitted with a biased shorter-period orbit. We highlight nine candidates with brown-dwarf companions for preferential follow-up. One candidate companion around the Sun-like star G 15-6 could be confirmed as a genuine brown dwarf using external radial-velocity data. This new approach is a powerful complement to the traditional identification methods for substellar companions among *Gaia* astrometric orbits. It is particularly relevant in the context of *Gaia* DR4 and its expected exoplanet discovery yield.

Key words: planets and satellites: detection – brown dwarfs – binaries: general – astrometry – methods: data analysis – surveys

1 INTRODUCTION

The third *Gaia* data release (DR3, [Gaia Collaboration et al. 2016, 2023a](#)) delivered the first uniform and large-scale census of astrometric binaries and increased the number of available orbital solutions by two orders of magnitude from a few thousand ([Mason et al. 2001](#)) to ~170 000. The revolutionary accuracy of *Gaia* made it possible to determine a large number of astrometric orbits with semi-major axes smaller than 1 milli-arcsecond (mas) for the first time ([Halbwachs et al. 2023](#)), finally opening the astrometric exoplanet-science window widely. However, small semi-major axes do not necessarily imply low companion masses: because the DR3 astrometric orbits usually refer to the unresolved photocentre of a binary, the principal astrophysical false-positive scenario for an exoplanet candidate is a nearly equal-mass and equal-brightness binary star (e.g. [Gaia Collaboration et al. 2023b; Marcussen & Albrecht 2023](#)).

The astrometric orbits of several known giant exoplanets have been determined in DR3 ([Holl et al. 2023; Gaia Collaboration et al. 2023b; Winn 2022](#)), leading to better constraints on their orbital configurations and masses. *Gaia* DR3 also contains a number of new

giant exoplanet candidates from astrometry.¹ The default procedure to confirm those is to gather additional data, e.g. spectroscopy and precision radial-velocities (RV), that exclude any false-positive scenario.

Here we propose an intermediate step to identify the most promising exoplanet candidates that can be prioritised for follow-up. Our machine learning approach relies only on DR3 without the need for external datasets. Because of the very small number of confirmed exoplanets with DR3 orbits, which we need to ‘train’ our models, we use as proof-of-concept the identification of substellar companions in general, i.e. both extrasolar planets and brown-dwarf companions. Since the mass distribution of substellar companions is structured but continuous (e.g. [Grether & Lineweaver 2006; Sahlmann et al. 2011](#)), this does not imply a loss of applicability, but it conveniently doubles the size of the ‘training’ sample.

2 *Gaia* DR3 DATA SELECTION AND AUGMENTATION

We queried the `gaiadr3.nss_two_body_orbit` table and selected all astrometric orbits, i.e. entries having a `nss_solution_type` of

* E-mail: Johannes.Sahlmann@ext.esa.int (JS)

† E-mail: Pablo.Gomez@esa.int (PG)

¹ The *Gaia* exoplanet candidate list is at <https://www.cosmos.esa.int/web/gaia/exoplanets>

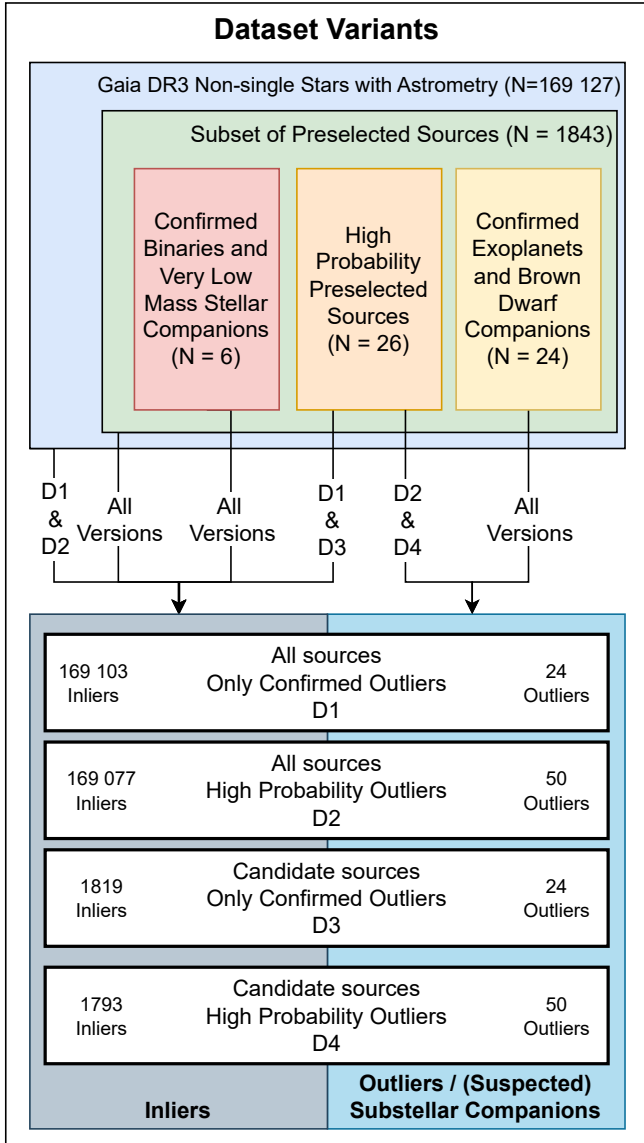


Figure 1. Overview of the data and different partitionings used. Source pre-selection was performed as described in Section 2.2.

either ‘Orbital’, ‘AstroSpectroSB1’, ‘OrbitalAlternative*’, or ‘OrbitalTargetedSearch*’.

For 98 sources that have both ‘AstroSpectroSB1’ and ‘OrbitalTargetedSearch*’ solutions we only retained the ‘AstroSpectroSB1’ solutions. Two solutions were identified as false positives by the *Gaia* collaboration² and we discarded those. This left us with 169 127 orbit solutions for the same number of sources.

For these sources, we retrieved the data of the *gaia_source* table which contains magnitudes, colours, radial velocities, and other information obtained from the astrometric single-star solution (Lindgren et al. 2021a).

The DR3 table fields are described in the online documentation (van Leeuwen et al. 2022), but not all are relevant for the purpose of

Table 1. Fill values used for data imputation. The table *nss_tbo* stands for *nss_two_body_orbit*, FV stands for *fill value*, and *N* indicates the number of values filled.

Table	Field	FV	Unit	N
gaia_source	radial_velocity	0	km/s	21460
gaia_source	radial_velocity_error	2.41	km/s	21460
gaia_source	phot_rp_mean_mag	12.67	mag	2
gaia_source	phot_bp_mean_mag	13.70	mag	2
gaia_source	bp_rp	0.99	mag	2
gaia_source	phot_bp_rp_excess_factor	1.22		2
nss_tbo	eccentricity_error	0		1979

our study. The selection of relevant fields and the augmentation with additional fields is described below.

The *gaia_source* and *nss_two_body_orbit* fields that we used are listed in Tables A1 and A2, respectively. We augmented these tables with a few fields to make relevant source or orbit parameters directly accessible and interpretable. For the *gaia_source* table, we computed the absolute source *G*-band magnitude from the apparent magnitude *phot_g_mean_mag* and the parallax ϖ_{ss} from *gaia_source* without zero-point correction (Lindgren et al. 2021b).

For the *nss_two_body_orbit* table, we converted the Thiele-Innes coefficients (*A, B, F, G*) into the geometric orbital elements (the semimajor axis of the photocentre orbit a_0 , the argument of periastron ω , the longitude of the ascending node Ω , and the orbital inclination i) using the linearised formulae described in Halbwachs et al. (2023); Gaia Collaboration et al. (2023b); Holl et al. (2023) and taking into account all parameter covariances using code implemented in *pystrometry* (Sahlmann 2019). We also computed the astrometric mass function in solar masses as described in Halbwachs et al. (2023, Eq. 13):

$$f_M = 365.25^2 \frac{a_0^3}{P^2 \varpi_{nss}^3}, \quad (1)$$

where P is the orbital period in days and ϖ_{nss} is the parallax from *nss_two_body_orbit* in mas. Finally we joined both tables on the source identifier *source_id*.

We note that the *nss_solution_type* is disregarded in the machine learning analysis. This is intentional because we want to apply our approach to purely astrometric orbits with as little selection effects as possible. A *nss_solution_type* = ‘AstroSpectroSB1’, for instance, implies that a compatible orbit was detected in two *Gaia* instruments at the same time, and the necessary RV amplitude makes it unlikely that an exoplanet signature corresponds to a ‘AstroSpectroSB1’.

2.1 Data imputation

For some sources/solutions not all table fields have been filled, e.g. sources that are too faint to be observed with the *Gaia* Radial Velocity Spectrometer (RVS, Katz et al. 2023) do not have an entry in the *radial_velocity* field. We therefore filled these occurrences with appropriate numerical values. The affected fields and fill-values are listed in Table 1. The fill values were determined as the median of the remaining population, except for *radial_velocity* and *eccentricity_error* where they were set to zero.

² <https://www.cosmos.esa.int/web/gaia/dr3-known-issues#FalsePositive>

Table 2. Label counts for our dataset.

Label	Count
preselected sources	1787
high-probability preselected sources	26
brown_dwarf_companion	14
exoplanet	10
very_low_mass_stellar_companion	3
binary_star	3
false_positive_orbit	2

2.2 Definition of labels

To assign labels to individual sources and orbital solutions, we used the `binary_masses` table (Gaia Collaboration et al. 2023b, Sect. 5) and the literature.

131 142 of our selected sources have entries in `binary_masses`. 105 of those have several mass estimates stemming with different `binary_masses.combination_method`. We removed those listed as ‘SB2’ and ‘Eclipsing’ which left us with 131 037 unique sources. The preselected sources label was assigned to 1838 sources with `binary_masses.m2_lower` < 0.08 and the high-probability preselected sources label was assigned to sources with `binary_masses.m2_upper` < 0.08 (cf. Stevenson et al. 2023). In the context, the preselected sources label refers to solutions that correspond to sources, which based on their entries in `binary_masses` could be substellar-companion candidates.

Finally, we retrieved from the literature all the solutions that correspond to confirmed exoplanets (companion mass $M_2 \lesssim 20M_{\text{Jup}}$), brown-dwarf companions ($20M_{\text{Jup}} \lesssim M_2 \lesssim 80M_{\text{Jup}}$), and binary stars ($0.12M_{\odot} \lesssim M_2$), where within that last category we also marked very-low-mass stellar companions with $80M_{\text{Jup}} \lesssim M_2 \lesssim 0.12M_{\odot}$. Table 2 shows the label counts and Table A3 lists the individual solutions, their labels, and the respective references.

3 DATA ANALYSIS

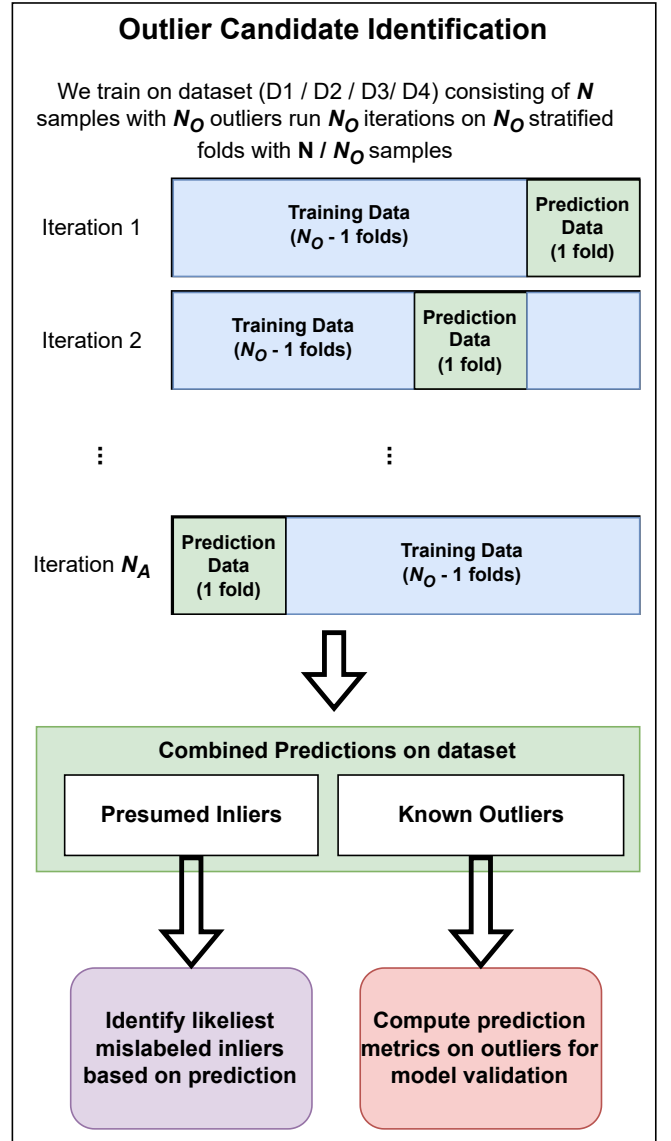
3.1 Substellar Companions as Anomalies

Fundamentally, we expect the number of substellar companions in the non-single sources to be quite small, in the range of less than one percent and in the single digit percentile range amongst the pre-selected sources. As such, we can consider them to be outliers in our data, as can be appreciated in Figure 3, and we expect them to be identifiable based on their DR3 parameters.

Even though some relations between the astrometric data, such as the value of the mass function f_M (see Equation 1), can be strongly indicative of the potential presence of a substellar companion, it is conceivable that there are various correlations and interactions between different parameters and the likelihood of a specific source having a substellar companion can likely not easily be reduced to a single parameter. Conversely, there are likely also other forms of outliers in the data, such as anomalies in the data processing pipeline or very low-mass stellar companions. Thus, we formulate the problem of identifying likely exoplanets and brown-dwarf companions as two-fold: first, in identifying outliers in the dataset and, secondly, identifying those outliers that are particularly likely to be substellar companions.

3.2 Semi-supervised Outlier Detection

Given the availability of some but few labelled examples (24 confirmed substellar companions), we choose a semi-supervised ma-

**Figure 2.** Overview of the algorithm used for identifying candidates.

chine learning approach, i.e. one that relies on a small number of labelled samples and a larger number of unlabelled samples during training. Further, given the difficulty of solving the task at all due to the limited amount of confirmed samples we consider different dataset partitionings in the training and ensemble across configurations as later explained in this section.

In particular, as shown in Figure 1, we build four dataset versions (D1, D2, D3, D4), which contain subsets of the data (e.g. only pre-selected sources in D3 and D4) and add 26 high-probability pre-selected sources as positively labelled outliers (D2 and D4).

In most established machine learning approaches (Zhao & Hryniewicki 2018; Han et al. 2022), the task of semi-supervised outlier detection is approached by training on the limited amount of data containing both known outliers and inliers and then predicting on a separate dataset. Since we only have a few confirmed outliers and virtually no confirmed inliers (i.e. binaries and very low mass stellar companions) we developed a different approach and instead consider our entire dataset of inliers (i.e. the vast majority of the data) to

be weakly labelled, i.e. potentially mislabelled. Thus, we transform the task from classifying newly unseen samples into inliers or outliers into identifying the likeliest mislabelled samples in our training data. To this end, we perform a k-fold cross-validation and use the predictions on the presumed inliers as the indication of whether we believe that sample to be a mislabelled one. This procedure is shown in detail in Figure 2. We choose the amount of folds to be identical to the number of outliers to maximise the amount of confirmed outliers in the training data. The left out outlier is used to compute the validation metrics in the results section.

To further improve the robustness of the approach and since precise performance evaluation is challenging with the limited amount of data, we use two different approaches in our ensembles. In particular, we utilise XGBoost (Chen & Guestrin 2016) as implemented in the Python package of the same name³ and a balanced random forest classifier (Chen et al. 2004) as implemented in the *imblearn*⁴ Python module. Given the invariance of both approaches to monotonous transforms, no data transforms were applied beyond the elimination of samples (i.e. sources/orbital solutions) missing any of the studied features.

3.3 Feature Selection and Importance

The original data contain a total of 47 unique data points per source (an overview of all parameters is given in Tables A1 and A2). During the development of the approach we used different feature-importance measures such as SHapley Additive exPlanations (SHAP) values (Lundberg & Lee 2017) and the feature importance implemented in *scikit-learn* (Pedregosa et al. 2011). Using this we identified and discarded several confounders, i.e. features that are marked as important for identifying outliers but that are not expected as such based on physical arguments.

As examples, we discarded both the parallax and the apparent magnitude of the source. These correlate positively with having confirmed substellar companions because those are the best-surveyed sources with ground-based, high-precision radial-velocity observations and generally are easier to follow-up. From an statistical astrophysical standpoint, there is little reason for a bright source to be more likely to host a substellar companion than a faint one, at least within the parameter space surveyed here. The other confounders that we identified are indicated in Tables A1 and A2.

Additionally, we use SHAP values as provided by the Python module⁵ of the same name to study the feature importance amongst our proposed candidates as well as to identify mislabelled training samples as shown in Section 4.

3.4 Ensembling and Candidate Selection

As outlined in the previous paragraphs, we use four different datasets (see Figure 1) and two different models (XGBoost and Balance-dRandomForest). From these, we build our predictions using max-voting on the 50 samples with the highest prediction as computed using the algorithm illustrated in Figure 2. We weight the voting relative to the chance to occur. Individual samples may, respectively, occur as inliers zero (confirmed substellar companions), two (high-probability preselected sources, orange in Figure 1), four

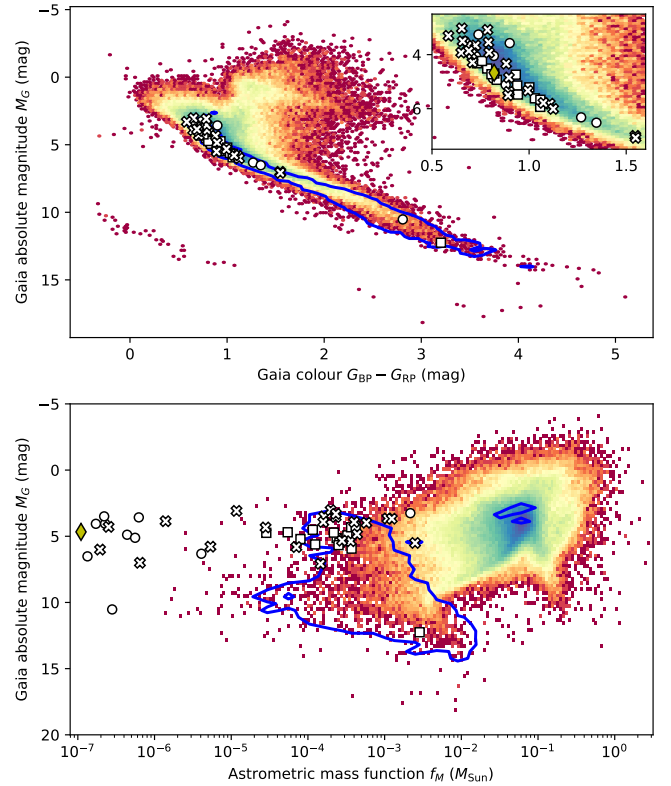


Figure 3. Density histograms of absolute magnitude as a function of colour (top panel, the inset show a zoom into the region of interest) and mass function (bottom) for all DR3 astrometric orbits. The blue contours indicate the concentration of the solutions labelled as preselected sources. Circles indicate the 10 confirmed exoplanets, squares indicate the 14 confirmed BD-companions, and crosses indicate our 22 best candidates for substellar companions discussed in the text. For reference, the Sun has $M_G = 4.67$ and $G_{BP} - G_{RP} = 0.82$ (Casagrande & VandenBerg 2018), and the mass function of a $5 M_J$ planet in a Jupiter-like orbit around the Sun is $1.1 \cdot 10^{-7}$. These reference locations are marked with a yellow diamond. The exoplanet with the largest mass function is HD 39392 b (Wilson et al. 2016; Stevenson et al. 2023).

(non-single sources) or eight (preselected sources) times. We measure the actual occurrence with three values: ρ which describes the rate of occurrence in the eight runs and ρ_{nss} and ρ_{ssc} , which are the rates of occurrence in the large datasets (D1 & D2) and smaller ones (D3 & D4), respectively.

4 RESULTS: SUBSTELLAR-COMPANION CANDIDATES

We applied a cutoff in relative occurrence at $\rho > 0.5$ which resulted in the identification of our 14 best candidates for exoplanets and brown-dwarf companions. In addition we identified four candidates with $\rho_{nss} > 0.5$ and four candidates with $\rho_{ssc} > 0.5$. These three categories are presented in their respective sections in Table 4. All 22 candidates are shown in Figure 3 and discussed below. We also identified lower-confidence candidates using a lower cutoff value of $\rho > 0.125$, which we list in Table A4.

³ <https://xgboost.readthedocs.io/en/stable/index.html> Accessed: 2024-03-08

⁴ <https://imbalanced-learn.org/> Accessed: 2024-03-08

⁵ <https://shap.readthedocs.io/en/latest/> Accessed: 2024-03-08

4.1 Validation

Ensuring the performance of our approach is a challenging task given the small amount of labelled samples. In the prediction method described in Figure 2 we obtain the predictions on the left-out fold as in a stratified K-fold validation. We use these predictions to compute performance metrics. As the inlier labels in these folds are weak labels (we expect some substellar companions in them) the metrics are probably underestimating the true performance since the models correctly "mislabel" some false inliers. Similarly, for the high probability (but not confirmed) outliers some may be mislabelled outliers, further impacting the performance measurements. Detailed results for different configurations are given in Table 3. Overall, we achieve very good results on the area under the receiver operating characteristic (AUROC) and accuracy of predictions. The area under the precision recall curve (AUPRC) results are worse but this is expected given the weak labels and significant class imbalance (less than 0.03% labelled outliers amongst all sources).

A secondary measure of the performance of our approach is the accuracy of the applied majority voting scheme to identify the best candidates from the eight configurations. A total of 170 unique sources show up in the top 50 outliers of the eight approaches (i.e. amongst all samples including presumed inliers and outliers). Among those 170, we find 22 of our 24 confirmed substellar companions among the 61 highest ranked samples across all configurations, each being identified in at least two separate runs. The only missing ones are the brown dwarf companions in LHS 1610 (*Gaia* DR3 43574131143039104, [Fitzmaurice et al. 2023](#)) and the brown dwarf in HD 89707 (*Gaia* DR3 3751763647996317056, [Gaia Collaboration et al. 2023b](#)). The one around LHS 1610 was likely missed due to the very-red colour of its M5-dwarf host star, which is uncommon in the confirmed substellar companions. The one around HD 89707 was barely below the detection threshold scoring highly on most models. We investigate this further in Section 4.4 on feature importance.

4.2 Exoplanet candidates

Table 4 is ordered by increasing mass function and we will discuss the individual systems here. We identified five high-probability exoplanet candidates. All of them are previously-known exoplanet candidates and have *Gaia* astrometric object of interest identifiers (*Gaia*-ASOI-#⁶):

The companion of HD 40503 (*Gaia*-ASOI-002, [Gaia Collaboration et al. 2023b](#); [Holl et al. 2023](#); [Marcussen & Albrecht 2023](#); [Winn 2022](#)) continues to await full RV confirmation. The companion of * 54 Cas (*Gaia*-ASOI-003) is an exoplanet candidate discussed in [Gaia Collaboration et al. \(2023b\)](#). The star BD+75 510 (HIP 66071, *Gaia*-ASOI-001, [Holl et al. 2023](#); [Gaia Collaboration et al. 2023b](#)) was followed up with high-precision RVs ([Sozzetti et al. 2023](#)) and a sub-Jupiter mass exoplanet was discovered. We also identify HD 128717 (*Gaia*-ASOI-009) as a strong candidate for hosting a super-Jupiter, motivating prioritised follow-up of this star.

The companion of BD+24 4592 (*Gaia*-ASOI-005) appears to be a strong exoplanet candidate in our analysis on the basis of the *Gaia* DR3 orbit, but this star was previously identified as spectroscopic binary (G 127–33, [Latham et al. 2002](#)) with a period of 3977 days and it is listed in the SB9 catalog ([Pourbaix et al. 2004](#)) with a large RV amplitude of 2.7 km/s. The *Gaia* astrometric period of 1009 days

is very close to the DR3 time range. It is therefore plausible that the *Gaia* orbit is spurious and the partially-covered binary-star orbit was interpreted as a low-amplitude orbit at $\sim 1/4$ of the true period. We therefore argue that *Gaia*-ASOI-005 should be re-classified as questionable.

4.3 Brown-dwarf companion candidates

We identified 17 brown-dwarf companion candidates with mass estimates spanning the brown-dwarf desert but predominantly located on the heavy side ($\geq 60 M_J$).

We identified the stars TYC 4998-437-1, BD+32 92, TYC 277-599-1, LP 769-9, HD 49264, HD 212620 as high-probability candidates for hosting brown-dwarf companions. For these six sources we did not find auxiliary information in the literature.

HD 207740 hosts a brown-dwarf companion candidate. Three Keck HIRES spectra of this source are discussed in [Rice & Brewer \(2020\)](#) but no RVs appear to have been published.

The stars HD 206484 and HD 78631 have DR3 solution types of ‘AstroSpectroSB1’ which means that the *Gaia* RVS also detected a compatible RV variation. The companion mass estimates from `binary_masses` in these cases are therefore more reliable and straddle the substellar boundary, i.e. these companions are either high-mass brown dwarfs or very-low-mass stars. For HD 78631 we noted a strong discrepancy between our companion-mass estimate ($\sim 123 M_{Jup}$, assuming a dark companion) and the one from `binary_masses` of $\sim 80 M_{Jup}$, which was determined using a non-zero flux ratio ([Gaia Collaboration et al. 2023b](#)).

The star HD 99251 hosts a brown-dwarf companion candidate. This star is also EPIC 201928968, a *Kepler* eclipsing binary candidate with orbital period < 1 day. No close companion was found with Speckle observations ([Schmitt et al. 2016](#)).

The source *Gaia* DR3 2540855308890440064 hosts a brown-dwarf companion candidate. This source_id is not resolved by Simbad and the source is a $10''$ visual binary with [TYC 4672-237-1](#).

Our analysis of the DR3 ‘OrbitalTargetedSearch’ orbit of HD 104289 indicates a very low-mass stellar companion in a ~ 1233 day orbit. The true period, however, is almost twice as long with ~ 2389 days as determined by ground-based RVs ([Kiefer et al. 2019](#)), who also detected the star’s orbit in *Hipparcos* astrometry at 2σ confidence. Furthermore, this source has an independent ‘SB1’ solution in the `nss_two_body_orbit` table with an even shorter period of ~ 886 d, i.e. about one quarter of the true period. The companion-mass estimate from `binary_masses` listed in Table 4 seems to have used parameters from the two incompatible DR3 solutions and therefore is inaccurate. As shown by [Kiefer et al. \(2019\)](#), the companion is indeed a very low-mass star and this is the second example in this work where the *Gaia* DR3 orbit is spurious because the binary’s motion had not yet been monitored long enough.

GSC 09436-01089 has a solution type of ‘AstroSpectroSB1’ which means that the *Gaia* RVS also detected a compatible RV variation. Using the primary-mass estimate of $M_1 = 1.16 \pm 0.12 M_\odot$ from `binary_masses` and resampling the DR3 orbit parameters while accounting for all covariances we obtain a companion-mass estimate of $M_2 = 74.88^{+9.20}_{-8.07} M_{Jup}$. GSC 09436-01089 B is therefore likely a high-mass brown dwarf but it may also be a very-low-mass star.

Our analysis of the HD 153376 astrometric orbit suggests that it is the likely host of a low-mass brown dwarf in a 910 day period. However, an extremely eccentric ($e \approx 0.8$) radial-velocity orbit of the same star was determined by [Kiefer et al. \(2019\)](#) with a period of ~ 4900 days and a minimum mass of $\sim 0.24 M_\odot$. Similarly to BD+24 4592 and HD 104289, this is the third case of a long-period

⁶ <https://www.cosmos.esa.int/web/gaia/exoplanets>

Table 3. Validation results for different configurations showing accuracy of prediction as well as area under the receiver operating characteristic (AUROC) and area under the precision recall curve (AUPRC).

Metric	Only Confirmed Outliers	High Probability Outliers	All Sources	Candidate Sources	XGBoost	Random Forest	All
Accuracy	0.97	0.94	0.98	0.96	0.99	0.92	0.96
AUROC	0.98	0.97	0.99	0.97	0.98	0.97	0.97
AUPRC	0.65	0.49	0.5	0.57	0.66	0.47	0.56

Table 4. Best candidates for exoplanets and brown-dwarf companions. The SpT column indicates the source’s spectral type as listed in Simbad, the solution type column indicates a short-hand for the `nss_solution_type` (similar to [Marcussen & Albrecht 2023](#): OTSV is ‘OrbitalTargetedSearchValidated’, OTS is ‘OrbitalTargetedSearch’, and ASB1 is ‘AstroSpectroSB1’), M_2 is a companion-mass estimate under the dark-companion assumption and using the primary-mass estimate M_1 from `binary_masses`, ρ is the relative occurrence introduced in Section 3.4, ρ_{nss} is the relative occurrence for dataset variants D1&D2 only, ρ_{ssc} is the relative occurrence for dataset variants D3&D4 only, the `ssc` flag is 1 when the solution was part of ‘preselected sources’ or ‘high-probability preselected sources’ and 0 otherwise, and $M_{2,\text{alt}}$ is the companion-mass range as estimated in `binary_masses`.

<i>Gaia</i> DR3 source_id	Name	SpT	sol. type	P (day)	f_M (M_\odot)	M_2 (M_{Jup})	ρ	ρ_{ssc}	ρ_{nss}	ssc	M_1 (M_\odot)	$M_{2,\text{alt}}$ (M_\odot)
2884087104955208064	HD 40503	K2V	OTSV	826.5	1.9e-07	5.2	0.8	0.8	0.8	1	0.79 $^{+0.05}_{-0.23}$	0.004-0.681
522135261462534528	* 54 Cas	F8	OTS	401.1	2.5e-07	7.1	0.9	1.0	0.8	1	1.09 $^{+0.06}_{-0.31}$	0.005-0.905
1712614124767394816	BD+75 510	M0V	OTSV	297.6	6.4e-07	7.3	0.8	0.8	0.8	1	0.71 $^{+0.05}_{-0.20}$	0.006-0.632
1610837178107032192	HD 128717	F8	OTS	1089.2	1.4e-06	12.8	0.9	1.0	0.8	1	1.13 $^{+0.06}_{-0.16}$	0.010-1.109
1878822452815621120	BD+24 4592	K2	OTS	1009.3	5.4e-06	16.3	0.9	1.0	0.8	1	0.82 $^{+0.05}_{-0.21}$	0.014-0.766
1897143408911208832	HD 207740	G5V	OTS	712.2	2.8e-05	32.3	0.9	1.0	0.8	1	0.99 $^{+0.05}_{-0.12}$	0.029-1.089
6330529666839726592	TYC 4998-437-1	—	Orbital	526.1	7.1e-05	39.0	0.6	0.5	0.8	1	0.82 $^{+0.03}_{-0.20}$	0.032-0.831
364792020789523584	BD+32 92	F8	OTS	291.9	1.6e-04	67.2	1.0	1.0	1.0	1	1.21 $^{+0.06}_{-0.14}$	0.057-1.382
5773484949857279104	GSC 09436-01089	—	ASB1	409.9	2.3e-04	73.8	0.6	0.8	0.5	1	1.16 $^{+0.07}_{-0.12}$	0.063-1.391
3913728032959687424	HD 99251	F5	Orbital	328.9	2.3e-04	78.6	0.9	1.0	0.8	1	1.28 $^{+0.06}_{-0.14}$	0.069-1.411
2540855308890440064	—	N/A	Orbital	239.8	2.8e-04	65.7	0.9	1.0	0.8	1	0.88 $^{+0.06}_{-0.17}$	0.056-1.006
1156378820136922880	G 15-6	G4	Orbital	268.3	3.6e-04	72.2	0.8	1.0	0.5	1	0.88 $^{+0.05}_{-0.30}$	0.065-0.872
217148973635565680	HD 206484	F8	ASB1	479.5	4.0e-04	90.4	0.8	1.0	0.5	1	1.18 $^{+0.06}_{-0.06}$	0.078 $^{+0.006}_{-0.006}$
3909531609393458688	TYC 277-599-1	—	Orbital	520.6	4.4e-04	79.5	0.8	1.0	0.5	1	0.92 $^{+0.06}_{-0.13}$	0.067-1.141
4545802186476906880	HD 153376	F8V	OTS	910.8	1.2e-05	24.2	0.4	0.0	0.8	0	NaN	NaN
5148853253106611200	LP 769-9	—	Orbital	339.6	1.5e-04	44.8	0.4	0.0	0.8	1	0.69 $^{+0.05}_{-0.19}$	0.039-0.723
3921176983720146560	HD 106888	F8	OTSV	366.3	5.8e-04	98.9	0.5	0.0	1.0	0	1.11 $^{+0.06}_{-0.14}$	0.083-1.388
3067074530201582336	BD-06 2423A	—	OTS	43.6	2.5e-03	155.8	0.4	0.0	0.8	0	NaN	NaN
5484481960625470336	HD 49264	G3V	Orbital	428.0	1.6e-04	59.7	0.5	0.8	0.2	1	1.02 $^{+0.06}_{-0.08}$	0.052-1.261
2280560705703031552	HD 212620	F8	Orbital	429.0	2.0e-04	76.1	0.4	0.8	0.0	1	1.32 $^{+0.06}_{-0.19}$	0.065-1.475
5323844651848467968	HD 78631	F8V	ASB1	666.5	1.1e-03	123.6	0.5	1.0	0.0	1	1.11 $^{+0.06}_{-0.06}$	0.076 $^{+0.014}_{-0.012}$
1576108450508750208	HD 104289	F8	OTS	1233.3	1.2e-03	132.7	0.5	1.0	0.0	1	1.15 $^{+0.06}_{-0.05}$	0.047 $^{+0.006}_{-0.006}$

binary orbit being mistaken for a shorter-period and small-amplitude signal by the *Gaia* data processing.

The astrometric orbit of HD 106888 has a compatible RV solution in terms of period and companion mass determined by [Kiefer et al. \(2019\)](#). This had already been realised by the *Gaia* team in charge of the relevant DR3 processing ([Holl et al. 2023](#)) who assigned this solution the type ‘OrbitalTargetedSearchValidated’. The companion mass is estimated at $\sim 0.1 M_\odot$, thus slightly above the substellar limit, yet our models have picked it up as an outlier in the D1&D2 runs with $\rho_{\text{nss}} = 1.0$. This companion has been detected directly (e.g. [Tokovinin et al. 2020](#)). For completeness, HD 106888 also has an outer, ultracool L1-dwarf companion at $\sim 38''$ separation ([Marocco et al. 2017](#)), which makes this a triple system.

Our models in the D1&D2 runs identified the orbit of BD-06 2423A as indicative of a substellar companion, however, the companion mass is estimated at $\sim 0.15 M_\odot$, i.e. quite above the substellar limit. This is also the candidate with by far the shortest orbital period of ~ 44 days. This star is also a wide binary with an entry in the Washington Double Star Catalogue ([Mason et al. 2001](#)), thus, this constitutes another triple system.

Finally, we present G 15-6 as the first independently-validated substellar companion identified by our work. The DR3 orbit implies a massive BD companion in a 268 day orbit. This source had already been identified as a possible brown-dwarf host from RV monitoring

by [Latham et al. \(2002\)](#) and it is listed in the SB9 catalogue with a period of 266 days. The matching periods and companion-mass estimates leave little doubt that the same orbital motion is detected both by *Gaia* and the RVs from [Latham et al. \(2002\)](#). Using the primary mass estimate of $M_1 = 0.67 M_\odot$ from [Latham et al. \(2002\)](#) with a 10 % uncertainty, and resampling the DR3 orbit parameters while accounting for all covariances we obtain a companion-mass estimate of $M_2 = 62.43^{+6.16}_{-5.44} M_{\text{Jup}}$. This companion therefore lies firmly in the substellar range and is the first confirmed brown-dwarf companion that was identified with our machine learning approach.

4.4 Feature Importance Results

In these section, we study the model predictions using SHAP values ([Lundberg & Lee 2017](#)) to identify both the reasons for the models’ predictions on the entire sample population and our candidate pool, but also for individual samples such as the confirmed brown dwarf the models missed.

4.4.1 Discussion of selected features

It is helpful to inspect the information content of a few features in more detail:

Mass function (f_M): A small mass function is a necessary condition for a system with a substellar companion⁷, but it is not a sufficient condition because twin-binary stars also have very small astrometric mass functions.

Radial-velocity error: As explained in the [online documentation](#) and [Katz et al. \(2023\)](#); [Babusiaux et al. \(2023\)](#), the RV error given in `gaia_source` has a stellar magnitude-dependent meaning. For bright sources (`phot_g_mean_mag` ≤ 13) it is derived from the uncertainty of the median of the RV timeseries. In that case, a large RV error can therefore stem from large individual RV uncertainties or from unmodelled RV variations, e.g. as present for a binary star. For faint sources (`phot_g_mean_mag` ≥ 13), the RV error is determined by stacking the individual cross-correlation functions and therefore the sensitivity to binary-induced motion is different (cf. [Andrew et al. 2022](#)). In the sample of $\sim 170\,000$ astrometric orbits with available RV error, about 43 % fall in the ‘bright’ category, and this percentage decreases to 36 % for the preselected sources. In addition to the bi-modal determination of the RV error, there is the general dependency on apparent stellar magnitude: the brighter the star, the higher the signal-to-noise in the spectra, and the smaller the RV error. As a result of these multiple dependencies it is often not directly interpretable how the RV error has influenced the models’ predictions.

Goodness-of-fit: The `goodness_of_fit` from `nss_two_body_orbit` corresponds to the ‘gaussianized chi-square’ statistic. For good orbital fits it should approximately follow a normal distribution with zero mean value and unit standard deviation. Values larger than roughly +3 indicate a bad fit. Our selection on astrometric orbits contains a mix of purely-astrometric orbits and combined RV+astrometric orbits, i.e. of type ‘AstroSpectroSB1’. For the latter, the `goodness_of_fit` refers to the combined fit, hence we can expect different feature characteristics between both groups.

Flux excess: the `phot_bp_rp_excess_factor` ([Riello et al. 2021](#)) contains a measure of the consistency between the red and blue source fluxes measured by *Gaia*. It has been shown that this metric can be sensitive to near-equal-brightness ($\Delta\text{mag} < 0.5$) binaries ([Belokurov et al. 2020](#)).

Colour and absolute magnitude: Finally, the *Gaia* colour $G_{BP} - G_{RP}$ ($\equiv \text{bp_rp}$) and absolute magnitude M_G ($\equiv \text{absolute_phot_g_mean_mag}$) indicate the location of the source in the colour-magnitude diagram (Fig. 3 top).

4.4.2 Predictions for populations

In terms of understanding the predictions on the entire population and the candidate pool, Figures 4 and 5 show the SHAP value distributions for the top five features of the candidates and a random sample of sources, respectively. The colour indicates the distribution of the feature, and especially smaller values of the variables are associated with higher SHAP values. It can be seen that identification as a likely candidate is influenced especially by small values of the mass function ($f_M \equiv \text{mass_function_msun}$) and/or small radial velocity errors.

A detailed look at individual SHAP values in association with `mass_function_msun` values is available in Figure 6 which highlights their complex interaction. Conversely, the random sample in Fig. 5 displays that most samples are ruled out as candidates by large `mass_function_msun` values and/or large radial velocity errors. The *Gaia* colour `bp_rp` of the source also seems to play a more important

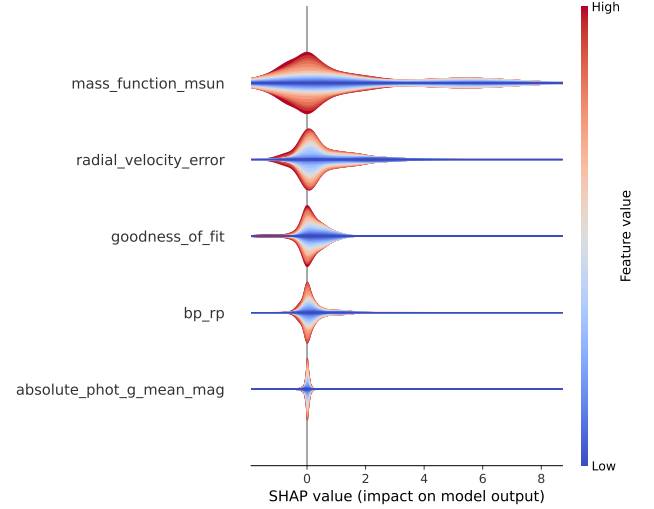


Figure 4. SHAP value distribution for the top five features of the top 50 sources identified in each of the 8 configurations (total number of 8×50 sources); colour indicates distribution of the feature; especially smaller values of the variables are associated with higher SHAP values.

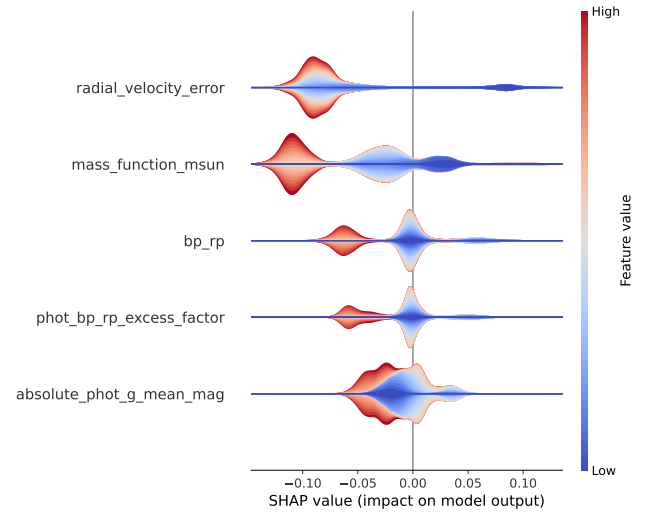


Figure 5. SHAP value distribution for the top five features of in a random sample of 50 sources per configuration; colour indicates distribution of the feature; especially larger values of the variables are associated with smaller SHAP values.

role here. Note, however the difference in magnitude on the x-axes of Figures 4 and 5. Additionally, Figure 6 also displays the distributions of SHAP values and `mass_function_msun` values in random samples of non-single source population and the preselected sources. Note that even though they feature small `mass_function_msun` values, these are not associated with large SHAP values in most preselected sources.

4.4.3 Predictions for individual systems

Investigating individual sources/solutions, we want to highlight three specific samples: The missed confirmed brown dwarf in

⁷ We do not discuss brown-dwarf binaries here.

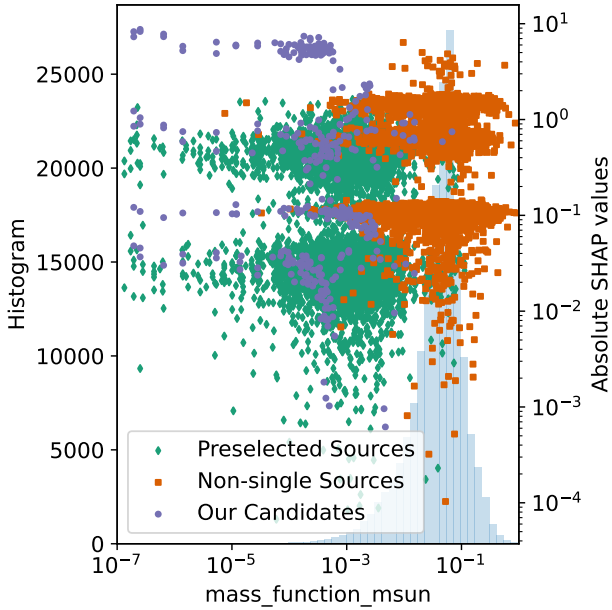


Figure 6. SHAP values for `mass_function_msun` of candidates and random samples (same samples as in Fig. 5) in relation to their `mass_function_msun` values and in the background a histogram of the value distribution in the non-single source population

LHS 1610, the top candidate around HD 40503, and *Gaia* DR3 246890014559489792 (*Gaia* object of interest identifier Gaia-ASOI-016), a small `mass_function_msun` outlier that was not identified as a candidate by our analysis. This can help us understand the decision process of the models, find potential confounders and help interpret the data of individual samples. In addition, decision plots for the missed brown dwarf around HD 89707 are in the Appendix in Figures A1 and A2. It was likely just barely below the detection threshold scoring highly on multiple models.

Figures 7 and 8 show decision plots for the missed brown dwarf around LHS 1610 for the random forest and XGBoost models, respectively. Here, the high radial-velocity error and `mass_function_msun` compared to other candidates such as HD 40503 are the main contributors to the decision. However, we can also see that the colour (`bp_rp` = 3.2) is a strong contributor, which makes sense as this is one of only two confirmed outliers with such a red colour - all others have `bp_rp` < 1.5 as seen in Figure 3. Overall, we can indeed see that with those characteristics the brown dwarf around LHS 1610 is atypical compared to the other confirmed brown dwarfs and exoplanets and the model’s decision process is stringent. A remedy to this mis-identification would be the inclusion of more labelled training samples like the confirmed brown dwarf around LHS 1610.

Figures 9 and 10 display the decision plots for the top exoplanet candidate around HD 40503 for the random forest and XGBoost models, respectively. The classification as outlier is driven by small values of the radial-velocity error and `mass_function_msun`. Notably, the `bp_rp` colour was not an important feature.

Finally, Figures 11 and 12 show the decision plots for *Gaia* DR3 246890014559489792. Looking at the small `mass_function_msun` value of $1.367\text{e-}6$ (cf. Figure 3) it would be conceivable that this is a strong candidate. However, as seen in the decision plots this is not

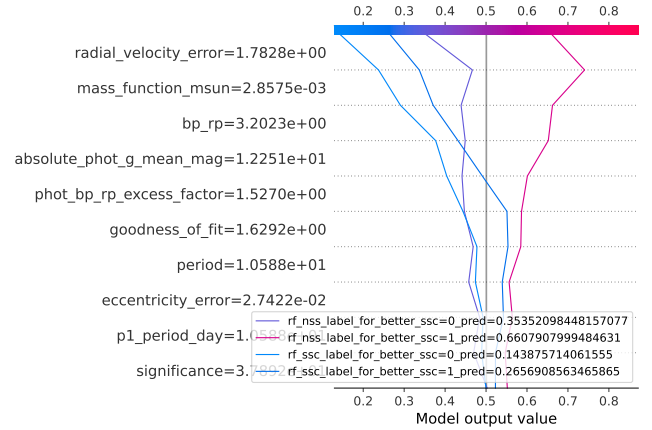


Figure 7. Decision plot showing feature contribution to model output for the random forest models for the brown dwarf in LHS 1610. Features are sorted by importance, feature values are shown on the left. A move of the line to the right in the row corresponding to a feature indicates a positive contribution to a classification as an outlier, i.e. exoplanet or brown dwarf, and vice versa.

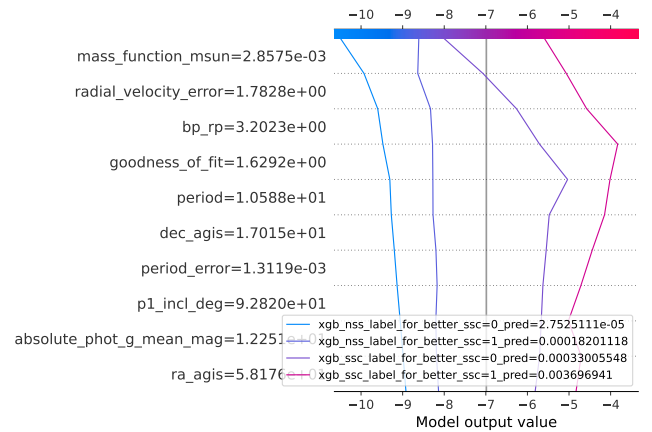


Figure 8. Decision plot showing feature contribution to model output for the XGBoost models for the brown dwarf in LHS 1610. Features are sorted by importance, feature values are shown on the left. A move of the line to the right in the row corresponding to a feature indicates a positive contribution to a classification as an outlier, i.e. exoplanet or brown dwarf, and vice versa.

the case because the other features, in particular the radial-velocity error, `bp_rp`, and goodness-of-fit contribute to an inlier classification.

Additional data and a full list of candidates are given in the Appendix.

5 DISCUSSION

The results shown in this work clearly indicate the viability of using a machine learning-based approach to identifying likely candidates for exoplanets and brown-dwarf companions. The majority of known exoplanets and brown-dwarf companions in the dataset were picked up successfully by the models and the identified new candi-

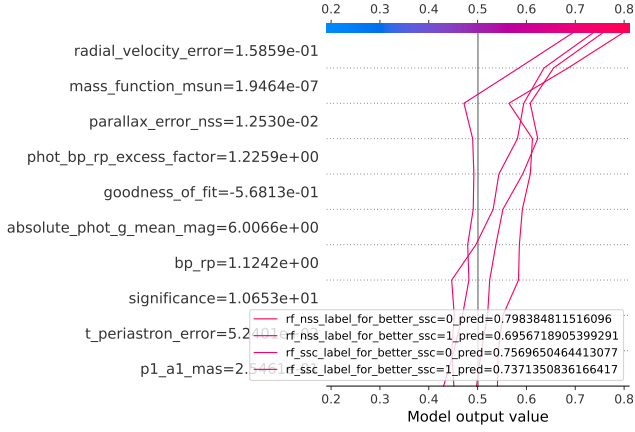


Figure 9. Decision plot showing feature contribution to model output for the random forest models for HD 40503. Features are sorted by importance, feature values are shown on the left. A move of the line to the right in the row corresponding to a feature indicates a positive contribution to a classification as an outlier, i.e. exoplanet or brown dwarf, and vice versa.

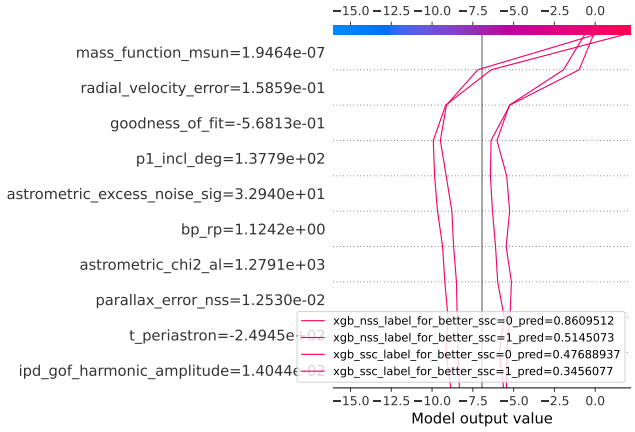


Figure 10. Decision plot showing feature contribution to model output for the XGBoost models for HD 40503. Features are sorted by importance, feature values are shown on the left. A move of the line to the right in the row corresponding to a feature indicates a positive contribution to a classification as an outlier, i.e. exoplanet or brown dwarf, and vice versa.

dates exhibit physical properties, such as expected companion mass, that indicate that they indeed are worthy of follow-up studies.

One predictable drawback of the approach in this regard is the tendency of identifying new candidates that mostly lie within the distribution of already-known candidates in terms of their features. For example, the location of our best candidates in the colour-magnitude diagram (Fig. 3 top) largely coincides with the region where the confirmed substellar companions, i.e. the training sample, resides. This is a common drawback of machine learning approaches and could be remedied by providing a richer ‘training’ dataset that, e.g., includes more confirmed substellar companions around redder sources ($bp_rp > 1.5$). In the same vein it has to be mentioned that the presented approach is of course greatly impacted by the very limited number of confirmed samples. These aspects will improve with time as the results of various DR3-orbit follow-up studies are being published and certainly with the release of *Gaia* DR4, when many more orbits of

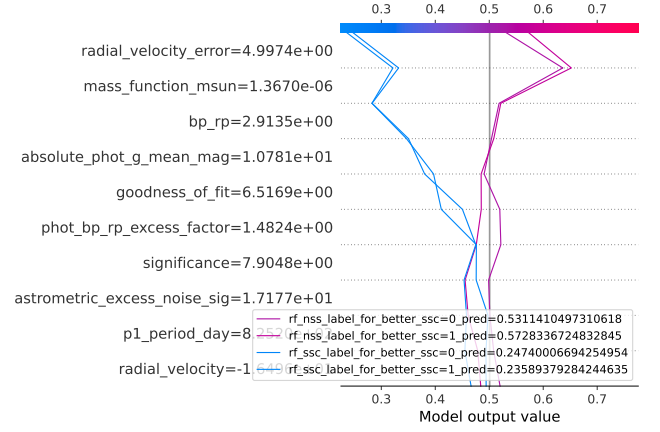


Figure 11. Decision plot showing feature contribution to model output for the random forest models for GaiaDR3 246890014559489792. Features are sorted by importance, feature values are shown on the left. A move of the line to the right in the row corresponding to a feature indicates a positive contribution to a classification as an outlier, i.e. exoplanet or brown dwarf, and vice versa.

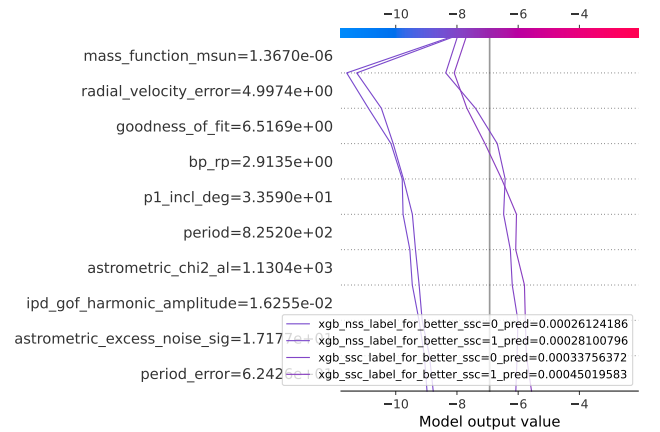


Figure 12. Decision plot showing feature contribution to model output for the XGBoost models for GaiaDR3 246890014559489792. Features are sorted by importance, feature values are shown on the left. A move of the line to the right in the row corresponding to a feature indicates a positive contribution to a classification as an outlier, i.e. exoplanet or brown dwarf, and vice versa.

stars with substellar companions will be released. We anticipate that the iterative identification and confirmation of an increasing number of exoplanets with *Gaia* orbits, covering growing areas in parameter space, will lead to a positive feedback loop with machine learning approaches, which will help to accelerate the pace of discoveries.

A particularly precious dataset for approaches like ours are small mass-function systems that actually are confirmed to be near-twin binaries (Marcussen & Albrecht 2023). These systems are crucial for *teaching* the models how to identify these astrophysical false positives. We therefore urge the teams involved in the observational follow-up of *Gaia* astrometric exoplanet candidates to publish their results, regardless of the outcome.

In terms of the performance and power of the presented approach several observations can be made. First, as displayed in Figures 4

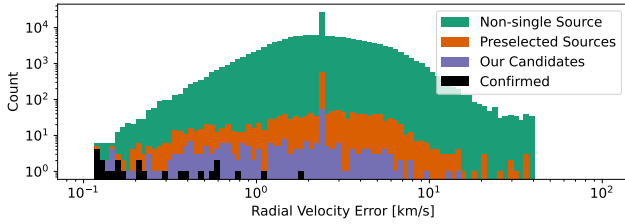


Figure 13. Distribution of radial velocity error in the sub-populations. The central peaks are caused by data imputation (Section 2.1) with the median for missing RV error values.

and 5, the decision making of the models is truly multivariate as different features can lead to the identification of likely outliers and different features can support either a classification as outlier or not. For example, the goodness-of-fit feature is the third strongest in identification of our candidates but does not appear among the random sample were instead `bp_rp` is third strongest.

Another indicator of such behavior can be seen in Figure 6. Even though `mass_function_msun` is the strongest feature overall (with small values being associated with a classification as outlier) a small value alone is not sufficient for a classification as outlier as exemplified by *Gaia* DR3 246890014559489792 and in Figures 11 and 12.

These kinds of observations are interesting for complementing a human-based analysis of the data since one can use the models’ identification of important features to identify and investigate potential confounders and spurious relationships in the data. In some cases, such as for the eliminated features like parallax and absolute source magnitude, this is trivial but in others it can inspire follow-up investigations.

The most obvious example of this is the `radial_velocity_error`. The models consistently identified it as a strong feature and, as displayed in Figure 13, there is a correlation between the presence of a confirmed exoplanet or brown-dwarf companion and a smaller `radial_velocity_error`. As explained in Section 4.4.1, this particular feature has a complex (expected) relation with the presence of orbital signatures. All hosts of confirmed substellar companions have RV errors smaller than the median value for astrometric orbits (Fig. 13). The same applies to almost all our identified candidates. The underlying reason is expected to be a mixture of outlier classification (for small RV errors) and inlier classification (for large RV errors that can be caused by unmodelled binary motion). A detailed investigation of these effects is outside the scope of this initial proof of concept. We note, however, that we performed ablation studies that indicated that our approach identifies similar candidates without the `radial_velocity_error` feature. Thus, even if this relationship is spurious, it should not compromise the performance of the presented approach.

6 CONCLUSIONS

We successfully demonstrated a new approach for identifying individual systems with particular properties, i.e. outliers, in the ensemble of *Gaia* DR3 astrometric orbits. As first application, we searched for the most likely sources orbited by extrasolar planets and brown dwarfs, but the approach could be adapted to other science cases, e.g. to search for black holes or twin binary stars instead.

Using machine learning, we identified 22 high-confidence sys-

tems with substellar companions, of which five host extrasolar-planet candidates that were previously known. One of the exoplanet candidates (BD+24 4592, *Gaia*-ASOI-005) is a false-positive because the *Gaia* orbit does not correspond to the true orbit of the system, which is a known RV binary.

We identified 17 high-confidence systems with brown-dwarf-companion candidates. Two of those candidates (HD 104289 and HD 153376) are false positives because the *Gaia* orbits do not correspond to the true orbits of the known RV binaries, and one candidate (BD-06 2423A) has in fact a low-mass stellar companion although it was picked up by our models. Three brown-dwarf companion candidates (HD 206484, HD 78631, GSC 09436-0108) have combined astrometric+RV orbital solutions (*‘AstroSpectroSB1’*) and the companions straddle the substellar-stellar mass boundary. The companion of HD 106888 is a very low-mass star.

The presence of a brown dwarf with an astrometric mass of $M_2 = 62.43^{+6.16}_{-5.44} M_{\text{Jup}}$ orbiting our high-confidence candidate G 15-6 was confirmed by literature RV measurements. We propose that the remaining nine high-confidence brown-dwarf companion candidates identified in this study be followed-up preferentially.

With *Gaia* we anticipate that machine learning analyses of astrometric orbits will grow into becoming powerful complements to the traditional approaches of cross-checking with existing data and literature and following-up with additional observations when pursuing specific scientific goals.

As the *Gaia* astrometric-orbit catalogue will grow significantly in DR4, machine learning approaches will become more and more important for prioritising follow-up and identifying interesting systems and ‘outliers’. In the same way, any analysis of the DR4 epoch data (*Gaia* astrometric timeseries of all sources will be released with DR4⁸) that has the goal of identifying non-single stars, e.g. through non-linear motions and drifts, single-, or multi-companion orbits, will have to address the problem of false-positives. The holistic machine learning approach that facilitates the use of as much information as available has many advantages in that respect. In particular, once sufficient training data will be available, it is very likely that machine learning algorithms will automatically identify a sizeable fraction of twin binary stars, which are the principal astrophysical false positives that affect *Gaia* astrometric planet searches.

As a byproduct of this study and as part of the validation of our best candidates we uncovered that the astrometric orbits for 3 out of 22 solutions ($\sim 14^{+10}_{-5} \%$ using binomial statistics) are false positives. They occurred when the *Gaia* DR3 astrometric exoplanet pipeline (Holl et al. 2023)⁹ processed the *Gaia* data collected over ~ 1000 days for sources that are large-amplitude binary stars with much-longer true periods between 2400 and 4900 days. The incomplete orbital arc was then fitted with a small-amplitude signal with a period shorter than the true period, which resulted in a candidate system with substellar companion. Whereas the tendency of astrometric pipelines to fit incompletely-covered orbits with short-period spurious orbital solutions has been discussed previously (Casertano et al. 2008; Holl et al. 2023), the particularly damaging effect this may have on small-amplitude solutions that can be mistaken for the signatures of exoplanets has to our knowledge not been documented before.

⁸ <https://www.cosmos.esa.int/web/gaia/release>

⁹ This pipeline produced only solutions of type *‘OrbitalTargetedSearch*’* and *‘OrbitalAlternative*’*.

Table A1. Used and computed fields for the `gaia_source` table. Instead of reproducing the field descriptions from [van Leeuwen et al. \(2022\)](#) here, we included a direct link to the online documentation.

Column	Description	Comment
<code>source_id</code>	online documentation	not used
<code>ra</code>	online documentation	
<code>dec</code>	online documentation	
<code>parallax</code>	online documentation	confounder
<code>parallax_error</code>	online documentation	
<code>pmra</code>	online documentation	confounder
<code>pmdec</code>	online documentation	confounder
<code>visibility_periods_used</code>	online documentation	
<code>radial_velocity</code>	online documentation	
<code>radial_velocity_error</code>	online documentation	
<code>astrometric_chi2_al</code>	online documentation	
<code>ipd_gof_harmonic_amplitude</code>	online documentation	
<code>bp_rp</code>	online documentation	
<code>phot_bp_rp_excess_factor</code>	online documentation	
<code>ruwe</code>	online documentation	
<code>phot_g_mean_mag</code>	online documentation	confounder
<code>phot_rp_mean_mag</code>	online documentation	
<code>phot_bp_mean_mag</code>	online documentation	
<code>astrometric_excess_noise_sig</code>	online documentation	
<code>astrometric_primary_flag</code>	online documentation	not used
<code>astrometric_excess_noise</code>	online documentation	
<code>astrometric_n_good_obs_al</code>	online documentation	
<code>absolute_phot_g_mean_mag</code>	absolute <i>G</i> mag	computed

Table A2. Used and computed fields for the `nss_two_body_orbit` table.

Column	Description	Comment
<code>source_id</code>	online documentation	not used
<code>nss_solution_type</code>	online documentation	not used
<code>ra</code>	online documentation	
<code>dec</code>	online documentation	
<code>parallax</code>	online documentation	confounder
<code>parallax_error</code>	online documentation	
<code>pmra</code>	online documentation	confounder
<code>pmdec</code>	online documentation	confounder
<code>period</code>	online documentation	
<code>period_error</code>	online documentation	
<code>t_periastron</code>	online documentation	
<code>t_periastron_error</code>	online documentation	
<code>eccentricity</code>	online documentation	
<code>eccentricity_error</code>	online documentation	
<code>astrometric_n_good_obs_al</code>	online documentation	
<code>obj_func</code>	online documentation	
<code>goodness_of_fit</code>	online documentation	
<code>efficiency</code>	online documentation	
<code>significance</code>	online documentation	
<code>p1_a0_mas</code>	a_0 (mas)	computed
<code>p1_omega_deg</code>	ω (deg)	computed
<code>p1_OMEGA_deg</code>	Ω (deg)	computed
<code>p1_incl_deg</code>	i (deg)	computed
<code>mass_function_msun</code>	f_M (M_\odot)	computed

APPENDIX A: AUXILIARY TABLES

This paper has been typeset from a \LaTeX file prepared by the author.

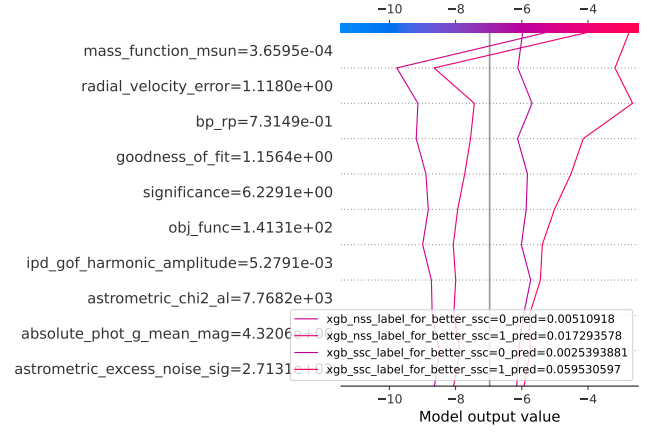
**Figure A2.** Decision plot showing feature contribution to model output for the XGBoost models for the brown dwarf in HD 89707. Features are sorted by importance, feature values are shown on the left. A move of the line to the right in the row corresponding to a feature indicates a positive contribution to a classification as an outlier, i.e. exoplanet or brown dwarf, and vice versa.

Table A3. Assigned labels

Gaia DR3 source_id	Name	label	Reference
2047188847334279424	HD185501	binary_star	Horch et al. (2020)
5122670101678217728	HD12357	binary_star	Marcussen & Albrecht (2023)
2052469973468984192	Ross 1063	binary_star	Marcussen & Albrecht (2023)
68502955838335168	HD77065	brown_dwarf_companion	Gaia Collaboration et al. (2023b)
3751763647996317056	HD89707	brown_dwarf_companion	Gaia Collaboration et al. (2023b)
3750881083756656128	HD91669	brown_dwarf_companion	Gaia Collaboration et al. (2023b)
3309006602007842048	HD30246	brown_dwarf_companion	Gaia Collaboration et al. (2023b)
2778298280881817984	HD5433	brown_dwarf_companion	Gaia Collaboration et al. (2023b)
2651390587219807744	BD-004475	brown_dwarf_companion	Gaia Collaboration et al. (2023b)
5563001178343925376	HD52756	brown_dwarf_companion	Gaia Collaboration et al. (2023b)
824461960796102528	HD82460	brown_dwarf_companion	Gaia Collaboration et al. (2023b)
43574131143039104	LHS1610	brown_dwarf_companion	Fitzmaurice et al. (2023)
1035000055055287680	HD68638A	brown_dwarf_companion	Unger et al. (2023)
5999024986946599808	CD-4610046	brown_dwarf_companion	Unger et al. (2023)
1181993180456516864	HD132032	brown_dwarf_companion	Unger et al. (2023)
873616860770228352	BD+291539	brown_dwarf_companion	Gaia Collaboration et al. (2023b)
855523714036230016	HD92320	brown_dwarf_companion	Gaia Collaboration et al. (2023b)
6421118739093252224	HD175167	exoplanet	Gaia Collaboration et al. (2023b)
3424193536079703808	HD39392	exoplanet	Stevenson et al. (2023)
2603090003484152064	GJ876	exoplanet	Gaia Collaboration et al. (2023b)
4976894960284258048	HD142	exoplanet	Gaia Collaboration et al. (2023b)
637329067477530368	HD81040	exoplanet	Gaia Collaboration et al. (2023b)
5855730584310531200	HD111232	exoplanet	Gaia Collaboration et al. (2023b)
2367734656180397952	BD-170063	exoplanet	Gaia Collaboration et al. (2023b)
4745373133284418816	HR810	exoplanet	Gaia Collaboration et al. (2023b)
1594127865540229888	HD132406	exoplanet	Gaia Collaboration et al. (2023b)
4062446910648807168	HD164604	exoplanet	Gaia Collaboration et al. (2023b)
4698424845771339520	WD 0141-675	false_positive_orbit	Cosmos Pages
5765846127180770432	HIP 64690	false_positive_orbit	Cosmos Pages
5266148569447305600	HD42936	very_low_mass_stellar_companion	Barnes et al. (2020)
1224551770875466496	HD140913	very_low_mass_stellar_companion	Unger et al. (2023)
4753355209745022208	HD17155	very_low_mass_stellar_companion	Unger et al. (2023)

Table A4. All 66 lower-confidence candidates selected as having $0.125 < \rho \leq 0.5$. Columns are the same as in Table 4.

<i>Gaia</i> DR3 source_id	Name	SpT	sol. type	<i>P</i> (day)	<i>f_M</i> (<i>M_⊙</i>)	<i>M₂</i> (<i>M_{Jup}</i>)	ρ	ρ_{ssc}	ρ_{nss}	ssc	<i>M₁</i> (<i>M_⊙</i>)	<i>M_{2,alt}</i> (<i>M_⊙</i>)
932447162423519232	UCAC4 684-047911	M2.3	ASB I	407.6	1.2e-05	18.0	0.2	0.0	0.5	0	0.63 ^{+0.05} _{-0.13}	0.150-0.639
4632430611684633344	HD 14717	G0V	Orbital	778.4	1.4e-05	27.2	0.2	0.5	0.0	1	1.10 ^{+0.03} _{-0.10}	0.022-1.208
4652393894560537728	HD 31251	G2V	ASB I	419.8	8.1e-05	46.6	0.2	0.0	0.5	0	NaN	NaN
2098419251579450880	2MASS J18405933+3950016	—	Orbital	241.7	8.9e-05	36.3	0.2	0.2	0.2	1	0.65 ^{+0.16} _{-0.16}	0.029-0.936
2984269003840680832	BD-15 1060	G5	Orbital	424.9	9.5e-05	52.2	0.2	0.5	0.0	1	1.09 ^{+0.06} _{-0.09}	0.045-1.291
3205578257602278784	TYC 4730-512-1	—	Orbital	598.1	9.7e-05	49.1	0.2	0.2	0.2	1	0.98 ^{+0.06} _{-0.09}	0.041-1.171
2994437527894182272	HD 42606	K3V	OTS	800.1	9.8e-05	46.4	0.2	0.0	0.5	0	0.90 ^{+0.05} _{-0.16}	0.516-0.984
5981932494567274368	CD-51 9508	G8	ASB I	413.9	1.0e-04	48.7	0.2	0.5	0.0	1	0.96 ^{+0.06} _{-0.06}	0.044 ^{+0.008} _{-0.008}
4854976609869179648	CD-41 1115	G5	ASB I	406.5	1.2e-04	50.6	0.2	0.5	0.0	1	0.94 ^{+0.06} _{-0.06}	0.068 ^{+0.008} _{-0.009}
2217319511295868672	BD+62 1950	F8	Orbital	596.0	1.2e-04	60.7	0.4	0.5	0.2	1	1.20 ^{+0.07} _{-0.14}	0.054-1.362
4598289263814843136	4598289263814843136	N/A	Orbital	435.8	1.4e-04	45.2	0.2	0.2	0.2	1	0.71 ^{+0.05} _{-0.21}	0.040-0.726
5671384265738137984	2MASS J0952219-192431	M7Ve	Orbital	278.5	1.5e-04	16.8	0.2	0.2	0.2	1	0.15 ^{+0.05} _{-0.05}	0.046-0.226
2744694491118490752	BD+05 5218	G0	ASB I	248.0	1.7e-04	59.4	0.2	0.5	0.0	1	0.98 ^{+0.06} _{-0.06}	0.042 ^{+0.005} _{-0.005}
1543883104727682176	TYC 3456-251-1	—	Orbital	593.3	1.7e-04	55.8	0.2	0.2	0.2	1	0.88 ^{+0.05} _{-0.30}	0.050-0.827
6604510475374443392	6604510475374443392	N/A	Orbital	761.5	1.9e-04	57.2	0.2	0.2	0.2	1	0.88 ^{+0.06} _{-0.14}	0.048-1.025
5077267349557463680	TYC 6437-159-1	—	Orbital	436.1	2.0e-04	61.3	0.2	0.2	0.2	1	0.95 ^{+0.06} _{-0.09}	0.054-1.168
30879908147741229920	TYC 198-493-1	—	Orbital	722.6	2.0e-04	56.1	0.4	0.5	0.2	1	0.83 ^{+0.05} _{-0.27}	0.047-0.812
5488452086658908544	HD 65577	F0IV	Orbital	678.3	2.1e-04	85.7	0.2	0.2	0.2	1	1.54 ^{+0.05} _{-0.19}	0.072-1.719
1856067303769195648	HD 340935	G2	Orbital	1176.2	2.1e-04	63.3	0.2	0.5	0.0	1	0.97 ^{+0.06} _{-0.06}	0.058 ^{+0.006} _{-0.006}
6500589824638636416	HD 219145	F5V	Orbital	316.0	2.1e-04	73.9	0.2	0.5	0.0	1	1.21 ^{+0.06} _{-0.19}	0.065-1.342
766977465670727936	HD 100360	K0	OTS	572.1	2.3e-04	66.7	0.2	0.0	0.5	0	NaN	NaN
4189636354105111168	TYC 5733-1115-1	—	ASB I	947.1	2.5e-04	68.5	0.2	0.0	0.5	0	NaN	NaN
273199953420523648	TYC 3734-75-1	—	Orbital	391.5	2.6e-04	64.4	0.2	0.2	0.2	1	0.88 ^{+0.05} _{-0.30}	0.056-0.854
5144739739589028992	LP 769-41	—	Orbital	150.8	2.9e-04	47.2	0.2	0.2	0.2	1	0.52 ^{+0.05} _{-0.17}	0.064-0.589
4224582166524567040	4224582166524567040	N/A	Orbital	413.7	2.9e-04	50.8	0.4	0.2	0.5	1	0.58 ^{+0.05} _{-0.17}	0.045-0.657
4668056781289612928	CD-69 203	—	ASB I	429.0	3.1e-04	79.8	0.2	0.5	0.0	1	1.11 ^{+0.05} _{-0.11}	0.070-1.357
6574387911224287488	L 499-75	M3	OTS	240.3	3.3e-04	50.0	0.5	0.5	0.5	1	0.53 ^{+0.05} _{-0.18}	0.045-0.597
1973932545092255616	TYC 3196-1933-1	—	Orbital	402.0	3.3e-04	81.5	0.4	0.5	0.2	1	1.11 ^{+0.06} _{-0.09}	0.070-1.393
5905528909017796480	5905528909017796480	N/A	Orbital	606.6	3.4e-04	72.3	0.4	0.5	0.2	1	0.92 ^{+0.06} _{-0.19}	0.062-1.050
2717981134566374272	V* V335 Peg	F5	OTS	787.7	3.5e-04	90.0	0.5	0.5	0.5	1	1.25 ^{+0.06} _{-0.14}	0.079-1.500
2347301645624022784	CD-25 215	—	Orbital	474.2	3.6e-04	78.4	0.2	0.2	0.2	1	1.00 ^{+0.06} _{-0.17}	0.066-1.182
2042732453670353664	2042732453670353664	N/A	Orbital	497.0	3.6e-04	72.9	0.2	0.2	0.2	1	0.89 ^{+0.06} _{-0.14}	0.062-1.077
6717694064902244224	TYC 7922-716-1	—	ASB I	288.7	3.6e-04	68.5	0.5	0.5	0.5	1	0.81 ^{+0.05} _{-0.06}	0.067 ^{+0.012} _{-0.012}
4503350935885071872	TYC 1557-2079-1	—	Orbital	462.6	3.7e-04	82.6	0.4	0.5	0.2	1	1.07 ^{+0.06} _{-0.10}	0.074-1.362
5501729312336121856	UCAC2 9182345	—	ASB I	130.3	3.8e-04	62.2	0.5	0.5	0.5	1	0.68 ^{+0.05} _{-0.05}	0.061 ^{+0.010} _{-0.010}
2214819118774573440	BD+68 1377	G0	ASB I	310.9	4.2e-04	81.3	0.2	0.5	0.0	1	0.97 ^{+0.06} _{-0.06}	0.081 ^{+0.009} _{-0.010}
4474368187335444352	TYC 438-609-1	—	Orbital	508.1	4.3e-04	79.4	0.4	0.5	0.2	1	0.93 ^{+0.05} _{-0.14}	0.068-1.143
1378974777381950080	TYC 3061-368-1	—	Orbital	309.3	4.5e-04	77.2	0.2	0.5	0.0	1	0.87 ^{+0.05} _{-0.30}	0.069-0.837
6827680034091744896	HD 203771	K1V	OTS	1105.4	4.5e-04	73.0	0.2	0.2	0.2	1	0.80 ^{+0.05} _{-0.19}	0.065-0.920
4984264505688458112	UCAC4 245-001421	—	ASB I	196.7	4.6e-04	80.0	0.5	0.5	0.5	1	0.91 ^{+0.06} _{-0.06}	0.075 ^{+0.009} _{-0.010}
6228661976111571072	HD 131197	K2III/IV	Orbital	421.0	4.8e-04	79.0	0.4	0.2	0.5	1	0.87 ^{+0.05} _{-0.15}	0.070-1.063
5538678297515561088	CD-38 3568	—	ASB I	267.6	5.0e-04	87.4	0.5	0.5	0.5	1	1.00 ^{+0.06} _{-0.07}	0.088 ^{+0.013} _{-0.014}
4390684426062198528	TYC 413-602-1	—	ASB I	240.9	5.1e-04	86.5	0.2	0.5	0.0	1	0.96 ^{+0.06} _{-0.07}	0.073-1.280
1693282786205650560	2MASS J12114960+7752445	—	Orbital	651.2	5.2e-04	54.3	0.2	0.2	0.2	1	0.47 ^{+0.05} _{-0.17}	0.048-0.548
6186817449775754496	PM J13128-2603	—	ASB I	87.0	5.2e-04	64.2	0.2	0.2	0.2	1	0.60 ^{+0.05} _{-0.05}	0.075 ^{+0.013} _{-0.013}
6345830951689788672	CPD-85 499	G5	ASB I	485.0	5.7e-04	92.8	0.2	0.5	0.0	1	1.01 ^{+0.06} _{-0.07}	0.080 ^{+0.012} _{-0.012}
5829002521785164160	TYC 9040-2811-1	—	ASB I	508.3	6.4e-04	107.3	0.2	0.5	0.0	1	1.19 ^{+0.06} _{-0.06}	0.087 ^{+0.014} _{-0.015}
4188152322648398592	2MASS J19262435-1045398	—	Orbital	175.8	7.0e-04	49.8	0.2	0.2	0.2	1	0.34 ^{+0.05} _{-0.16}	0.043-0.422
548478735430284416	BD+74 118	K5V	OTS	48.1	7.6e-04	86.9	0.4	0.5	0.2	1	0.78 ^{+0.05} _{-0.21}	0.078-0.920
5344309621263564160	TYC 8631-835-1	—	ASB I	789.9	7.7e-04	97.0	0.2	0.5	0.0	1	0.92 ^{+0.05} _{-0.06}	0.078 ^{+0.009} _{-0.009}
6012944872855490944	HD 139096	G3V	ASB I	129.5	8.3e-04	104.6	0.2	0.2	0.2	1	1.00 ^{+0.06} _{-0.06}	0.079 ^{+0.009} _{-0.009}
4441168914767115360	HD 153402	K0	OTS	104.2	8.4e-04	96.1	0.2	0.0	0.5	0	0.87 ^{+0.05} _{-0.19}	0.088-1.071
3063883403860016512	TYC 4858-1465-1	—	ASB I	328.7	9.4e-04	102.4	0.2	0.0	0.5	0	0.90 ^{+0.05} _{-0.05}	0.101 ^{+0.015} _{-0.016}
4725142772167859840	L 127-40	—	ASB I	118.8	1.1e-03	96.2	0.2	0.2	0.2	1	0.74 ^{+0.06} _{-0.05}	0.084 ^{+0.013} _{-0.012}
3067929881523376384	TYC 4854-2258-1	—	ASB I	262.7	1.1e-03	117.0	0.2	0.0	0.5	0	0.99 ^{+0.06} _{-0.06}	0.182 ^{+0.040} _{-0.038}
1003812373374277248	HD 49039	G5	OTS	19.9	1.5e-03	117.4	0.2	0.0	0.5	0	0.87 ^{+0.06} _{-0.21}	0.100-1.122
4955501899980809088	TYC 7548-325-1	—	ASB I	337.3	1.8e-03	125.2	0.2	0.2	0.2	1	0.86 ^{+0.06} _{-0.06}	0.082 ^{+0.013} _{-0.013}
5247111556405603840	TYC 8952-212-1	—	ASB I	402.4	2.2e-03	126.2	0.2	0.5	0.0	1	0.76 ^{+0.06} _{-0.05}	0.098 ^{+0.020} _{-0.019}
5612492292661869824	HD 60666	K1III	OTS	29.1	2.3e-03	150.3	0.2	0.0	0.5	0	NaN	NaN
2743198605549406464	HD 223238	G5V	OTS	61.3	2.5e-03	157.9	0.2	0.0	0.5	0	1.01 ^{+0.06} _{-0.10}	0.133-1.364
6911090115750857344	SCR J2108-0600	—	ASB I	144.1	2.9e-03	144.0	0.2	0.5	0.0	1	0.81 ^{+0.05} _{-0.05}	0.094 ^{+0.015} _{-0.015}
798068905726303232	* 11 LMi	G8Va	OTS	27.1	3.0e-03	156.2	0.2	0.0	0.5	0	0.91 ^{+0.05} _{-0.11}	0.137-1.182
6795834500861297408	SIPS J2049-2800	sdM6.5?	Orbital	641.1	3.1e-03	52.0	0.2	0.2	0.2	1	0.15 ^{+0.05} _{-0.07}	0.065-0.348
3931991608291720192	TYC 880-843-1	—	ASB I	257.6	3.4e-03	184.5	0.2	0.5	0.0	1	1.10 ^{+0.06} _{-0.06}	0.093 ^{+0.016} _{-0.015}
845583819682861184	LSPM J1131+5627	—	Orbital	392.5	1.3e-02	84.1	0.2	0.2	0.2	1	0.12 ^{+0.05} _{-0.05}	0.080 ^{+0.019} _{-0.018}
5207515806222756480	CPD-81 193	—	ASB I	71.8	1.5e-02	292.0	0.2	0.5	0.0	1	0.92 ^{+0.05} _{-0.05}	0.080 ^{+0.017} _{-0.016}